HHS Public Access

Author manuscript

ACS Appl Mater Interfaces. Author manuscript; available in PMC 2019 February 14.

Published in final edited form as:

ACS Appl Mater Interfaces. 2016 March 02; 8(8): 5137–5147. doi:10.1021/acsami.5b11936.

Diffusion-Weighted Magnetic Resonance Imaging for Therapy Response Monitoring and Early Treatment Prediction of Photothermal Therapy

Guifeng Fu[†,‡], **Lei Zhu**[†,‡], **Kai Yang**[§], **Rongqiang Zhuang**[‡], **Jin Xie**[*,⊥,‖], and **Fan Zhang**[*,‡]

[‡]State Key Laboratory of Molecular Vaccinology and Molecular Diagnostics & Center for Molecular Imaging and Translational Medicine, School of Public Health, Xiamen University, Xiamen, Fujian 361005, China

[§]Jiangsu Key Laboratory for Carbon-Based Functional Materials and Devices, Institute of Functional Nano and Soft Materials Laboratory (FUNSOM), Soochow University, Suzhou, Jiangsu 215123, China

[⊥]Department of Chemistry, University of Georgia, Athens, United States

[‖]Bio-Imaging Research Center, University of Georgia, Athens, United States

Abstract

Photothermal therapy (PTT) as a relatively new cancer treatment method has attracted worldwide attention. Previous research on PTT has focused on its therapy efficiency and selectivity. The early prognosis of PTT, which is pivotal for the assessment of the treatment and the therapy stratification, however, has been rarely studied. In the present study, we investigated diffusion-weighted magnetic resonance imaging (DW-MRI) as a tool for therapy monitoring and early prognosis of PTT. To this end, we injected PEGylated graphene oxide (GO-PEG) or iron oxide deposited graphene oxide (GO-IONP-PEG) to 4T1 tumor models and irradiated the tumors at different drug-light intervals to induce PTT. For GO-IONP-PEG injected animals, we also included therapy arms where an external magnetic field was applied to the tumors to improve the delivery of the nanoparticle transducers. DW-MRI was performed at different time points after PTT and the tumor apparent diffusion coefficients (ADCs) were analyzed and compared. Our studies show that photothermal agents, magnetic guidance, and drug-light intervals can all affect PTT treatment efficacy. Impressively, ADC value changes at early time points after PTT (less than 48 h) were found to be well-correlated with tumor growth suppression that was apparent days or weeks later. The changes were most sensitive to conditions that can extend the survival for more than 4 weeks, in which cases the 48 h ADC values were increased by more than 80%. These studies demonstrate for the first time that DW-MRI can be an accurate prognosis tool for PTT, suggesting an important role it can play in the future PTT evaluation and clinical translation of the modality.

[*]**Corresponding Authors** jin.xie@uga.edu., sailfmri@hotmail.com.

Author Contributions

†G.F. and L.Z. contributed equally. The manuscript was written through contributions of all authors. All authors have given approval to the final version of the manuscript.

The authors declare no competing financial interest.

Graphical Abstract

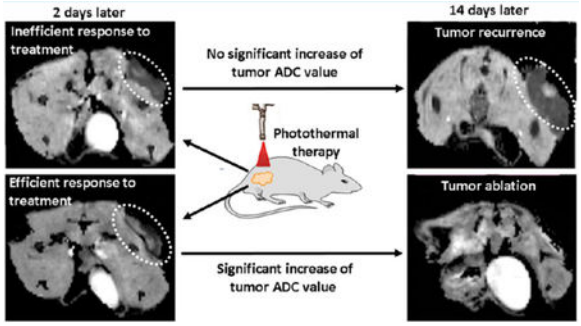

Keywords

photothermal therapy; graphene oxide; iron oxide; diffusion-weighted magnetic resonance imaging; apparent diffusion coefficient

INTRODUCTION

Photothermal therapy (PTT) has emerged as an important treatment modality. PTT uses light absorbing materials as transducers; these transducers, often in the form of nanoparticles, are delivered to tumors prior to the treatment and under photoirradiation, causing thermal ablation of cancer cells.[1] Compared to conventional treatment modalities, PTT affords the advantages such as minimal invasiveness and high selectivity. Moreover, PTT can be applied repeatedly without causing cumulative toxicity.[2] In the past decade, many nano-materials, such as gold nanoparticles,[3,4] carbon nanotubes (CNTs),[5,6] nanoparticulate graphene oxide (GO),[7,8] and upconversion nanocrystals (UNCs),[9] have been investigated as PTT agents. Among the candidate transducers, GO has attracted much recent attention.

GO is a two-dimensional, monolayer structure that can be made into nanoscale sheets of various sizes.[10] GO has all of the prerequisites for a good PTT agent, including strong and broad absorbance in the near-infrared red (NIR) spectrum window,[11] low toxicity,[12] biocompatibility[13,14] and good water stability.[15] Meanwhile, GO affords with multiple surface carboxyl groups, which allow for facile loading of drug molecules, stealth polymers, and other functionalities onto the sheet surface.[16–19] For instance, recent studies showed that iron oxide nanoparticles (IONPs) can be grown in situ onto the surface of GO.[20] The IONP deposits not only enhance the light-to-heat conversion efficiency of GO, but also enable them to be magnetically guided to tumors for improved therapy selectivity.[21,22]

So far, studies on GO-mediated PTT, or PTT in general, assess tumor response, almost exclusively, by measuring tumor sizes. However, tumor suppression is not the only important factor to be considered in the evaluation of treatment efficacy. In an era that emphasizes more and more on personalized medicine, it is paramount to tailor the intensity of a treatment to individual patients; pertaining to the subject,[23] there is a need of a methodology that can predict the therapy efficacy before or shortly after the treatment as opposed to weeks or months later. A number of noninvasive imaging techniques, including near-infrared

spectroscopy,[24] photoacoustic imaging,[25] and ultrasound imaging,[26] have been proposed as methods to monitor therapy response after PTT. Moreover, progress has been made to understand the relationship between temperature distribution and treatment outcomes.[27,28] Despite the efforts, however, there is a still lack of a predicative diagnosis tool for PTT.

We herein explored the feasibility of using diffusion-weighted magnetic resonance imaging, also known as DW-MRI, to monitor tumor response after GO-mediated PTT. DW-MRI has been increasingly used in the clinic to assess the extent of tissue damage after treatment. Apparent diffusion coefficient (ADC), a quantitative parameter of DW-MRI, is found to be able to assess tumor tissue ischemia, necrosis, or cellular lysis that is often seen after effective therapy and shows up long before apparent morphology changes.[29–34] Cheng et al. observed that ADC can clearly depict the thermal damage ring after microwave focal thermal therapy and suggested DW-MRI a better tool to predict tissue necrosis than contrast-enhanced imaging.[35] More recently, Pilatou et al. demonstrated that ADC changes can be used to delineate tissues damage after treatment by MRI-guided focused ultrasound surgery (MRgFUS).[36] Despite the great potential, however, DW-MRI has rarely been investigated to monitor tumor treatment after PTT.

In the present study, we injected GO or IONP-laden GO into 4T1 bearing mice and photoirradiated the tumors at different drug-light intervals to initiate PTT. For IONP-laden GO, we also included a therapy arm where an external magnetic field was applied to tumors for magnet-guided delivery of the nano-transducers. From the MRI results, it is evident that magnetic guidance led to more efficient accumulation of IONP-laden GO in tumors. DW-MRI was performed at different time points after the treatment and the tumor ADC value changes were monitored. We observed significantly an increase of ADC value within 48 h after the PTT, and the amplitude of the increase was well correlated with the treatment efficacy. Impressively, a dramatic increase of ADC value (>80%) was found to be associated with effective tumor growth suppression and extended animal survival that were apparent only weeks after the PTT. These results suggest ADC as an effective early prognosis marker for PTT, which is of great value for future development and clinical translation of the technology.

2. MATERIALS AND METHODS

2.1. Materials.

N-(3-(Dimethylamino)propyl-N-ethylcarbodii-mide) hydrochloride (EDC) was purchased from J&K Company (Beijing, China). NH_2-polyethylene glycol was purchased from Shanghai Seebio Biotech (Shanghai, China). Iron(III) chloride hexahydrate was purchased from Sinopharm Chemical Reagent Co., Ltd. (Shanghai, China). Dulbecco's modified Eagle medium (DMEM) was purchased from Thermo Scientific (Beijing, China). Fetal bovine serum (FBS) and antibiotics were purchased from PAA (Chalfont St Giles, U.K.). MTT assay kit, hyaluronidase and 4, 6-diamidino-2-phenylindole (DAPI) were purchased form Bioengineering Co., Ltd. (Shanghai, China). Calcein-AM was purchased from Invitrogen (Grand Island NY). Propidium iodide (PI) was purchased from Sigma-Aldrich Co. (St. Louis, MO). Glass bottom cell culture dishes were purchased from NEST Biotechnology Co. LTD (Nanjing, China). Cell culture dishes, Eppendorf tubes (1.5 mL), 6-well chambers

and 96-well flat-bottomed plates were purchased from JET BIOFIL (Guangzhou, China). 4T1 cell were purchased from ATCC (Manassas, VA).

2.2. Synthesis of GO-IONP-PEG.

GO and IONP deposited GO were synthesized by following a previously reported method.[37] To improve the biocompatibility and aqueous solubility, the particles were modified with poly(maleicanhydride-*alt*-1-octadecene) (C18PMH–PEG) according to a published procedure[38] to yield GO-PEG or GO-IONP-PEG. Briefly, 25 mg of C18PMH–PEG was added into in a solution of GO-IONP (1 mg/mL, 5 mL), and the solution was ultrasonicated for 5 min at room temperature. Five mg EDC was then added to the mixture and the solution was magnetically stirred overnight. The final product (GO-PEG or GO-IONP-PEG) was purified by a Millpore ultrafiltration tube (MWCO = 100 kDa) for 4 times and redispersed in deionized water.

2.3. Materials Characterization.

The stability of GO-IONP-PEG in water, saline, cell medium and serum was monitored visually at 37 °C for 48 h. UV–vis–NIR absorption spectra were recorded by a spectrophotometer (Multiskan GO, USA). The TEM images were taken by a JEM-2100 microscope (JEOL, JAPAN) at an accelerating voltage of 200 kV. Atomic force microscopy (AFM, Veeco Instruments Inc., Santa Barbara, USA) was used to analyze the morphology of the particles. The transverse relaxivity R_2 were measured on a 9.4T MRI scanner. For photothermal effect evaluation, GO-PEG, GO-IONP-PEG (both were 30 μg/mL), and PBS in 150 μL Eppendorf tubes were each irradiated with a NIR laser (808 nm, Stone laser, Shenzhen) at a fluence rate of 0.5 W/cm^2 for 10 min. Thermal images were obtained real-time by an FLIR A35-series camera (FLIR Systems Inc., Wilsonville, OR) and quantified by BM_IR software.

2.4. Cellular Uptake Study and Cell Cytotoxicity.

Approximately 5×10^3 4T1 cells were seeded in each well of a chamber slide (Lab-Tek Chamber Slide System) for 24h before the toxicity study. These cells were incubated with GO-IONP-PEG (100 μg/mL) for 0, 0.5, 1, 2, and 4 h and stained with Prussian blue staining kit and examined by a biological microscope (Nikon DS-Fi2, Japan). MRI phantom study was performed with cells that had been incubated with GO-IONP-PEG for 0, 0.5, 1, 2, and 4 h. After being washed thrice with PBS, the cells were dispersed in 100 μL 1.5% agarose gel in 150 μL Eppendorf tubes for MR images.

For cell cytotoxicity evaluation, 4T1 cells (5×10^3 cells per well) were seeded into 96-well plates and incubated with various con-centrations of GO-IONP-PEG for 24 h. After washing cells with PBS, cell cytotoxicity was studied by a standard MTT assay protocol. The relative cell viability was calculated by the following formula: relative cell viability (%) = absorbance of the treatment group/absorbance of the control group ×100%.

2.5. In Vitro Photothermal Therapy and Magnetic Targeting.

To investigate the cancer cell killing efficiency of GO-PEG and GO-IONP-PEG under laser irradiation, we seeded 4T1 cells (5000 cells per well) in 96-well plates and incubated with

GO-PEG or GO-IONP-PEG at the same GO concentration (100 μg/mL) at 37 °C for 12 h. The incubation medium was replenished and the cells were then irradiated with a NIR laser (808 nm) at different fluence rates (0.5 W/cm^2, 1.0 W/cm^2, 1.5 W/cm^2, and 2.0 W/cm^2) for 10 min. The cell viability was measured by MTT assays.

In vitro magnetic targeting experiments were performed by placing a NdFeB magnet (3000Gs) under the center of a 35 mm culture dish grown with 4T1 cells (1×10^5 cells). Into the culture dish GO-IONP-PEG (100 μg/mL) was added. After incubation for 4 h and washed 3 times with PBS, the cells were irradiated by an 808 nm NIR laser (1.0 W/cm^2 for 5 min). Dead and live cells were stained with Calcein AM (4 μM) and PI solutions (4 μM), respectively. Lastly, the cells were washed with PBS three times and observed under a fluorescence microscopy.

2.6. Biodistribution.

BALB/c mice (4–6 week old, 18–20 g, female) were purchased from Shanghai Slac Laboratory Animal CO. Ltd. All experiments were conducted according to protocols approved by the Animal Care and Use Committee (CC/ACUCC) of Xiamen University. To obtain 4T1 murine breast tumor model, 5×10^6 4T1 cells suspended in PBS (100 μL) were subcutaneously injected onto the back of each mouse. Studies were performed on these mice about 2–3 weeks later when the tumor volumes approached 70–80 mm^3.

For biodistribution studies, 10 mice bearing 4T1 tumors were randomized into two groups (n = 5). All the mice were intravenously injected with 200 μL of GO-IONP-PEG (1.5 mg/mL). For the magnetic targeting group, an NdFeB magnet (3000Gs) was attached to the skin of the tumors for 24 h. T_2-weighted and T_2-map MR images were taken before and 6, 12, and 24 h after the particle injection. In order to assess nanoparticle accumulation in the tumors and the liver, R_2 relaxivities at different time points were analyzed. Four hours after particle injection, all the mice were sacrificed and livers and tumors were removed and sliced for Prussian blue staining.

2.7. Tumor Photothermal Therapy and Assessment of Therapeutic Response.

Fifty 4T1 tumor bearing mice were randomly divided into ten groups (n = 10): (a) PBS with laser, (b) GO-PEG with laser (6 h postinjection), (c) GO-IONP-PEG with laser (6 h postinjection), (d) GO-IONP-PEG with laser (6 h postinjection) under an external magnetic field (MF), which was achieved by attaching a NdFeB magnet (3000 Gs) to the skin of the tumors for 6 h, (e) GO-PEG with laser (12 h postinjection), (f) GO-IONP-PEG with laser (12 h postinjection), (g) GO-IONP-PEG with laser (12 h postinjection) under MF for 12 h, (h) GO-PEG with laser (24 h postinjection), (i) GO-IONP-PEG with laser (24 h postinjection) and (j) GO-IONP-PEG with laser (24 h postinjection) under MF for 24 h. When the tumor volumes approached 70–80 mm^3, 200 μL of PBS, GO-PEG (1.5 mg/mL), or GO-IONP-PEG (1.5 mg/mL) were intravenously injected. All of the animals were irradiated by an 808 nm laser (2 W/cm^2 for 5 min) at designated time points. Thermal images were obtained in real-time by a FLIR A35 camera and quantified by BM_IR software. Mice were monitored for up to 60 days post PTT treatment for tumor regrowth and survival. The body weights of all mice were recorded every other day.

For therapeutic response assessment, T_2-weighted MRI and DW-MRI was performed before and at different times after PTT therapy (1, 2, 3, 7, 10, and 14 days). Tumor size was measured with a caliper tool to the nearest millimeter. More T_2-weighted images and ADC value. The tumor volumes were calculated using $AB^2/2$, where A is the largest and B is the smallest diameter of a tumor.

2.8. MR Data Acquisition and Analysis.

All phantom and animal MRI studies were performed on a 9.4 T small animal MRI scanner (Bruker 94/20, Germany). For animal studies, all the mice were anesthetized with 1.5% isoflurane/O_2 mixture and placed in a stretched prone position. MR images were acquired using the following parameters: (1) T_2WI: using turbo RARE sequence, TR = 2500, TE = 33 ms, field of view = 4 × 4 cm, matrix = 256 × 256, slice thickness = 1 mm, FA = 180, 9 contiguous slices; (2) T_2-map: using multislice multiecho (MSME) sequence, TR = 2500 ms, field of view = 4 × 4 cm, matrix = 256 × 256, FA = 180°, slice thickness = 1 mm, 9 contiguous slices, TE = 11, 22, 33, 44, 55, 66, 77, 88, 99, 110, 121, 132, 143, 154, 165, and 176 ms; (3) DW-MRI: using spin echo DW sequence, TR = 3000, TE = 27 ms, field of view = 4 × 4 cm, matrix = 128 × 128, FA = 90°, slice thickness = 1 mm, 9 contiguous slices, b values = 0, 1000s/mm^2.

T_2 maps and ADC maps were calculated on a pixel-by-pixel basis using the built-in software (Paravision 5.1, Bruker). Regions of interests (ROIs) were manually drawn across images. The T_2 relaxivity and a mean ADC was obtained from each ROI. The transverse relaxivity R_2 were calculate from the following equation: $R_2\left(t\right) = \frac{1}{T_2\left(t\right)}$, The increase in R_2 relaxivity caused by the presence of GO-IONP-PEG and GO-IONP-PEG with magnetic targeting in tumor at time t was calculated as a percentage prescan relaxivity value: $\mathrm{d}R_2\left(\%\right) = \frac{R2(t) - R2(0)}{R2(0)} 100\,\%$.[39] The ADC values were measurement by the Paravision 5.1 software, which were calculated from the DWI data sets according to the equation: $\mathrm{ADC} = -\frac{1}{b}\ln\left(\frac{S_i}{S_0}\right)$,[40] where S_i is the DWI signal intensity acquired at a certain diffusion gradient (b value) and S_0 is the baseline signal when b equals 0.[40] The percentage of ADC changes (ΔADC%) was computed using the equation: $\Delta\mathrm{ADC}\left(\%\right) = \frac{\mathrm{ADC}(n) - \mathrm{ADC}(0)}{\mathrm{ADC}(0)} 100\,\%$, where ADC(0) was the tumor ADC value prior to PTT and ADC(n) the ADC value on day n after PTT.[41]

2.9. Histological Analysis and Image Analysis.

For better assessment of the tumor therapy response, one mouse from each group was sacrificed 48 h after PTT and tumor was removed for histological analysis. The tumors were cut into two halves. Half one were fixed in a 4% formaldehyde solution, processed routinely into paraffin, sliced at 10 μm, stained with hematoxylin and eosin (H&E) and observed under a microscope. Another half of the tumor was imbedded in O.C.T. compound, sliced into 4-μm-thick sections, and fixed with cold acetone for 20 min for CD31 staining. Briefly, slices was blocked with 1% BSA for 30 min, incubated with rat antimouse CD31 primary antibody diluent (1:50) for 2 h at room temperature in a humid chamber, washed with PBS,

incubated with antirat IgG secondary antibody solutions for 30 min at room temperature. After washing with PBS, the whole slides were mounted with a DAPI-containing mounting medium and observed under a fluorescence microscope (Leica, Germany). CD31 positive vessels were quantitatively analyzed using the ImageJ software.

For evaluating if there were PTT-induced changes to the organs, the major organs including the heart, spleen, lung, liver, kidneys, and muscles were also collected for H&E staining.

2.10. Statistical Analysis.

Experiment results were analyzed as mean ± SD. Statistical analysis was performed using one-way ANOVA followed by Bonferroni multiple comparison test with $p < 0.05$ considered statistically significant.

3. RESULTS AND DISCUSSION

3.1. Preparation and Characterizations of GO-IONP-PEG.

The preparation of IONP-laden GO is illustrated in Scheme 1. GO was first synthesized following a published protocol.[42] IONPs were grown subsequently onto the surface of GO through hydrolysis of $FeCl_3$.[43] To improve the stability, we PEGylated the resulting nanoparticles with poly(maleicanhydride-*alt*-1-octadecene), or C18PMH–PEG (Scheme 1). The obtained conjugates (hereafter referred to as GO-IONP-PEG), were highly stable in water, saline, cell growth medium, and whole serum (Figure 1a). Transmission electron microscopy (TEM) analysis confirmed that the surface of GO were adorn with 5–10 nm IONPs (Figure 1b). The hydrodynamic size of GO-IONP-PEG, according to atomic force microscopy (AFM), was ~50 nm (Figure 1c), which agrees well with the previous reports.[21] GO-IONP-PEG showed broad absorbance in the visible and NIR spectrum ranges (Figure 1d). The absorbance is stronger than parental GO, which was attributed to the IONP deposits.[21]

The enhanced absorbance may translate to more prominent light-to-heat conversion efficiency. To investigate, we prepared a GO-IONP-PEG solution (30 μg/mL, starting temperature ~30 °C) and irradiated it by an 808 nm laser (0.5 W/cm^2). For comparison, we also prepared a solution of PEGylated GO nanoparticles (GO-PEG, 30 μg/mL, starting temperature ~30 °C) and subjected it to the same photoirradiation conditions. GO-IONP-PEG clearly induced a greater photothermal effect, increasing the solution temperature to 55.5 °C within 5 min, compared to that of 44.8 °C for GO-PEG (Figure 1e, f).

The IONP deposits also granted GO-IONP-PEG with good magnetic properties. When a magnet was applied to a GO-IONP-PEG solution, the particles were quickly drawn to the magnet (Figure 1g). Moreover, MRI phantom studies observed a clear, concentration-dependent T_2 shortening effect with GO-IONP-PEG (Figure 1h). On the basis of the phantom study results, it was deduced that the transverse relaxivity rate (i.e., r_2) for GO-IONP-PEG is 54.03 mM^{-1} s^{-1} (Figure 1i).

3.2. Cellular Uptake and Cytotoxicity.

Cell uptake studies were performed with 4T1 (murine breast cancer) cells. Prussian blue staining found a clear time-dependent uptake of GO-IONP-PEG, likely mediated by endocytosis (Figure 2a). The nanoparticle internalization can be monitored by MRI. Figure 2b shows a MRI phantom study with agarose samples of 4T1 cells that had been incubated with GO-IONP-PEG for different amounts of time. Corroborating with the Prussian blue staining results, an enhanced "darkening" effect was observed with cells that had endured long incubation times (Figure 2b).

Despite of the high uptake, GO-IONP-PEG induced little toxicity to cells in the dark. Even at a very high particle concentration (e.g., 240 μg/mL), 4T1 cells maintained over 80% viability (Figure 2c). The cell viability dropped significantly when the incubation was followed by 808 nm photoirradiation (Figure 2d), which is a hallmark of PTT-induced cell death. The PTT efficacy was irradiance dependent. For instance, at a GO-IONP-PEG concentration of 100 μg/mL and a fluence rate of 0.5 W/cm^2, 5 min photoirradiation decreased the cell viability to 42.85 ± 3.95% (Figure 2d). As a comparison, 2.0 W/cm^2 irradiation by the same amount of time dropped the viability to only 5.97 ± 1.64% (Figure 2d).

Next, we examined in vitro whether an external magnetic field can guide PTT to areas of interest. Specifically, a small magnet was placed right under the center of a cell culture dish grown with 4T1 cells (Figure 2e); into the incubation medium, GO-IONP-PEG (100 μg/mL) was added. Because of the presence of a magnetic field, the particles were attracted to the central area of the plate, manifesting as a black circle visible to the naked eyes (Figure 2e). After 4 h, the incubation medium was replenished and the 4T1 cells were washed by PBS; the whole plate was then irradiated by an 808 nm NIR laser for 5 min. Using an IR camera, we were able to monitor the temperature change in different areas of the plate (Figure 2e). Correlating with the particle distribution pattern, there was a radial temperature gradient. The highest temperature was found at the plate center and it was 56 °C. The cell viability was analyzed microscopically by calcein AM/propidium iodide (PI) assay (also known as live-and-dead assay). Reminiscent of the temperature pattern, cells lying in the central area of the plate were effectively killed by PTT (Figure 2e, red fluorescence), whereas those at the peripheral regions were minimally affected by the treatment (green fluorescence). In fact, there was a clear boundary between the live and dead zones, with the position of the boundary coinciding well with the GO-IONP-PEG distribution. These results suggest that GO-IONP-PEG-mediated PTT can be guided by an external magnetic field for selective cancer cell damage.

3.3. Magnet-Guided Tumor Targeting.

We next examined the efficiency of magnet-guided tumor targeting in vivo in 4T1 subcutaneous tumor models (n = 5). The animals were intravenously (i.v.) injected with GO-IONP-PEG (200 μL, 1.5 mg/mL). For the magnet field guided group (designated as GO-IONP-PEG+MF), an NdFeB magnet (3000 Gs) was attached to the tumor skin immediately after the particle injection. For comparison, animals were injected with GO-IONP-PEG but not applied with a magnet (GO-IONP-PEG). T_2-weighted MR images and T_2 maps were

acquired before and after the particle injection (Figure 3a, b). Region of interest (ROI) analysis was performed to assess the R_2 (i.e., $1/T_2$) changes in the liver and tumor (Figure 3c, d) at different time points. The GO-IONP-PEG group showed a certain degree of signal drop in tumors after the particle injection. Relative to the prescan, the percent R_2 increase (dR_2%) was 11.7, 16.71, and 37.18% at 6, 12, and 24 h, respectively (Figure 3d). The hypo-intensities were attributed to the accumulation of GO-IONP-PEG in tumors by the enhanced permeability and retention (EPR) effect.[44,45] The "darkening" effect was significantly enhanced in the GO-IONP-PEG+MF group (Figure 3b). Specifically, dR_2% was 22.19 and 45.49% at 6 and 12 h, and increased to a striking 60.81% at 24 h. The improved tumor accumulation was also confirmed by Prussian blue staining, which found more positive staining in tumors from the GO-IONP-PEG+MF group (Figure 3e).

3.4. In Vivo Photothermal Effect.

The in vivo photo-thermal effect was also studied in 4T1 tumor bearing BALB/c mice (n = 5). We injected GO-IONP-PEG, GO-IONP, or PBS to the animals (1.5 mg/mL for GO-IONP-PEG and GO-IONP). For GO-IONP-PEG, we again included a group where an external magnetic field was applied to the tumors after particle injection (GO-IONP-PEG +MF). For all of the animals, the tumors were irradiated by an 808 nm laser (2 W/cm^2, 5 min) at 6, 12, and 24 h after the injection. Tumor temperature was monitored in real time to assess the photothermal effect (Figure 4a).

Except for the PBS group, all of the animals showed a dramatic temperature increase in tumors (Figure 4b–d). It is noted that for all of the particle injected groups, the highest temperature was observed at 24 h (Figure 4b–d). This is likely attributable to the long circulation half-lives of GO-IONPs and GO-IONP-PEG, and hence the tumor accumulation was more efficient at late time points. At the same drug-light intervals, the GO-IONP-PEG +MF group always showed the most prominent temperature increase (Figure 4b–d). This is attributed to magnet-guided tumor targeting as well as the relatively high light-to-heat conversion efficiency of GO-IONP-PEG. In particular, for GO-IONP-PEG+MF with a drug-light interval of 24 h, the tumor temperature was increased to 65.19 °C within 5 min of photoirradiation (Figure 4d).

3.5. MRI to Monitor Photothermal Therapy.

Next, we conducted PTT tumor therapy studies with 4T1 tumor models and monitored the therapy response with both T_2 MRI and DW-MRI. The tumor growth, assessed on the basis of the T_2 maps (Figure 5a), was shown in Figure 5b–d. Relative to the PBS treated animals, the GO-IONP-PEG+MF, GO-IONP-PEG, or GO-IONP groups showed various degrees of tumor growth suppression (Figure 5b–d). The most effective treatment was observed with the GO-IONP-PEG+MF group and the best drug-light interval was 24 h. These results coincide with the photothermal study results (Figure 4). It is worth mentioning that for the GO-PEG and GO-IONP-PEG groups, the tumor growth was temporally arrested in the first week but then resumed in the second week (Figure 5b–d). As a comparison, GO-IONP-PEG +MF treatment with either a 12 or 24 h drug-light interval led to efficient tumor shrinkage, with the primary tumors almost disappeared after 2 weeks (Figure 5c, d).

The animals were scanned by DW-MRI at different time points post PTT (Figure 6a), and the mean ADC values in tumors were measured and compared (Figure 6b–d). Before PTT, the mean tumor ADC was $(0.582 \pm 0.038) \times 10^{-3}$ mm^2/sec. The number barely changed for the PBS group after photoirradiation (Figure 6b–d). As a comparison, GO-PEG, GO-IONP-PEG, and GO-IONP-PEG+MF groups all manifested significantly increased ADC values; interestingly, in all of the cases, ADCs values peaked at around day 2 and then dropped after day 3 (Figure 6b–d). On the basis of the observation, we computed percent ADC increase (ΔADC%) on day 1 and day 2 and compared the value among different treatment groups (Figure 6e–g). At the same drug-light intervals, the GO-IONP-PEG+MF groups always showed the largest ΔADC%, followed by the GO-IONP-PEG groups. In particular, for GO-IONP-PEG+MF with a 12 or 24 h drug light interval, the day-2 ΔADC% was striking, being 79.94 and 84.13%, respectively. These numbers were much higher than the other treatment conditions (Figure 6f, g). The ADC increase was mainly caused by PTT-induced necrosis, [46–48] which led to damaged cancer cell structures and thus increased water proton mobility. In our studies, an increase in the tumor uptake of GO-IONP-PEG was observed when a magnet was applied to tumors; the increase was more dramatic when the magnet was applied at the tumor site for longer times. These results suggest that magnetic guidance is beneficial to tumor targeting of GO-IONP-PEG and contribute to the great treatment efficacy which manifested higher ADC value. The ADC change was supported by H&E and CD31 staining with tumor tissues (taken 48 h after PTT, Figure 6h), which found extensive tumor necrosis and loss of vasculatures (Figure 6a) in the GO-IONP-PEG+MF groups (12 and 24 h drug-light intervals). Hence, it was no coincidence that the most dramatic ADC increase was observed in treatment groups associated with the most significant tumor growth suppression (Figure 5b–d).

The PTT-treated animals were monitored for up to 60 days. The animal survival results correlate to the therapy response observed in the first 2 weeks (Figure 7a). Compared to the control group, where all of the animals met a humane end point within 15 days, the PTT-treated animals all showed significantly improved survival. The longest survival was again observed with the two GO-IONP-PEG+MF groups (for both 12 and 24 h drug-light intervals), where 80% of the primary tumors were shrunk and showed no relapse for more than 60 days (Figure 7a). The treatment caused minimal systematic toxicity, which was supported by weight (Figure 7b) and H&E staining study results (Figure 7c).

4. CONCLUSION

PTT as a relatively new treatment modality has attracted wide attention. The treatment has shown great potential in clinical translation but much work is needed to optimize the treatment intensity and understand its side effects over repeated therapy sessions. Related to the topic is the variation of therapy response among individuals. Similar to conventional treatments, it is desired that PTT can be personalized so as to maximize treatment outcomes. To this end, a prognosis tool that can predict the long-term treatment efficacy would be highly valuable.

The present study suggests ADC value change as a prognosis biomarker for efficient PTT. In particular, we found that a dramatic ADC increase (>80%) in the first 48 h after PTT was

associated with treatments that would extend the survival of animals by more than 4 weeks. Notably, after treatment, the absolute ADC values in the peripheral regions of tumors were increased to above 1.000×10^{-3} mm^2/s. These observation echoes a recent study by Monguzzi et al., who found an optimal ADC cutoff of 1.277×10^{-3} mm^2/s for rectal cancer after radiochemotherapy.[49] These observations suggest the possibility of finding an ADC threshold that can be used to differentiate effective PTT treatments from those that are not. A few previous studies have investigated using DW-MRI to monitor prostate microwave focal thermal therapy and uterine fibroid MRgFUS.[35,36] The results suggest that DW-MRI is useful to delineate the treated regions[36] and better than contrast-enhanced imaging for accurate assessment of the eventual thermal damage.[35] Meanwhile, whether DW-MRI should be used as a stand-alone method or a complementary method needs to be assessed in future studies with more clinically relevant models.

Significant impact of drug-light interval and magnetic guidance on the efficacy of PTT was observed. Despite of the seemingly similar forms and doses of the transducers, the therapy outcomes varied largely among treatment groups. The observation suggests that while it is important to explore new photothermal agents, it is of equal importance to optimize the irradiation and delivery strategies for the best PTT efficacy.[50] Magnetic guidance also has proven to be effective in our studies to enhance PTT while inducing no additional side effects to the host. Whether the effect can be enhanced by a stronger magnetic field and/or a tumor targeting ligand will be investigated in our future studies.

In summary, we used DW-MRI to monitor GO-mediated PTT under different conditions. Our studies suggest that tumor ADC increase can serve as an accurate early prognosis marker for efficient PTT. DW-MRI as a therapy response and treatment prediction tool will find wide uses in future PTT studies and applications.

ACKNOWLEDGMENTS

This work was partially supported by the National Natural Science Foundation of China (NSFC) (81201086, 81471655 and 81301256, F.Z.), DoD CDMRP (CA140666, J.X.), a UGA-GRU seed grant (J.X.), and an Elsa U. Pardee Foundation Award (J.X.).

REFERENCES

References

(1). O′Neal DP; Hirsch LR; Halas NJ; Payne JD; West JL Photo-Thermal Tumor Ablation in Mice Using near Infrared-Absorbing Nanoparticles. Cancer Lett. 2004, 209 (2), 171–176. [PubMed: 15159019]

(2). Lal S; Clare SE; Halas NJ Nanoshell-Enabled Photothermal Cancer Therapy: Impending Clinical Impact. Acc. Chem. Res 2008, 41 (12), 1842–1851. [PubMed: 19053240]

(3). Huang X; El-Sayed IH; Qian W; El-Sayed MA Cancer Cell Imaging and Photothermal Therapy in the near-Infrared Region by Using Gold Nanorods. J. Am. Chem. Soc 2006, 128 (6), 2115–2120. [PubMed: 16464114]

(4). Jang B; Park JY; Tung CH; Kim IH; Choi Y Gold Nanorod-Photosensitizer Complex for near-Infrared Fluorescence Imaging and Photodynamic/Photothermal Therapy in Vivo. ACS Nano 2011, 5 (2), 1086–1094. [PubMed: 21244012]

(5). Ghosh S; Dutta S; Gomes E; Carroll D; D′Agostino R, Jr.; Olson J; Guthold M; Gmeiner WH Increased Heating Efficiency and Selective Thermal Ablation of Malignant Tissue with DNA-

Encased Multiwalled Carbon Nanotubes. ACS Nano 2009, 3 (9), 2667–2673. [PubMed: 19655728]

(6). Robinson JT; Welsher K; Tabakman SM; Sherlock SP; Wang H; Luong R; Dai H High Performance in Vivo near-Ir (>1 Mum) Imaging and Photothermal Cancer Therapy with Carbon Nanotubes. Nano Res. 2010, 3 (11), 779–793. [PubMed: 21804931]

(7). Geim AK Graphene: Status and Prospects. Science 2009, 324 (5934), 1530–1534. [PubMed: 19541989]

(8). Geim AK; Novoselov KS The Rise of Graphene. Nat. Mater 2007, 6 (3), 183–191. [PubMed: 17330084]

(9). Zhang L; Gao S; Zhang F; Yang K; Ma Q; Zhu L Activatable Hyaluronic Acid Nanoparticle as a Theranostic Agent for Optical/Photoacoustic Image-Guided Photothermal Therapy. ACS Nano 2014, 8 (12), 12250–12258. [PubMed: 25402600]

(10). Kim F; Cote LJ; Huang J Graphene Oxide: Surface Activity and Two-Dimensional Assembly. Adv. Mater 2010, 22 (17), 1954–1958. [PubMed: 20432227]

(11). Hontorialucas C; Lopezpeinado AJ; Lopezgonzalez JDD; Rojascervantes ML; Martinaranda RM Study of Oxygen-Containing Groups in a Series of Graphite Oxides - Physical and Chemical Characterization. Carbon 1995, 33 (11), 1585–1592.

(12). Schipper ML; Nakayama-Ratchford N; Davis CR; Kam NWS; Chu P; Liu Z; Sun X; Dai H; Gambhir SS A Pilot Toxicology Study of Single-Walled Carbon Nanotubes in a Small Sample of Mice. Nat. Nanotechnol 2008, 3 (4), 216–221. [PubMed: 18654506]

(13). Cheng C; Li S; Nie S; Zhao W; Yang H; Sun S; Zhao C General and Biomimetic Approach to Biopolymer-Functionalized Graphene Oxide Nanosheet through Adhesive Dopamine. Biomacromolecules 2012, 13 (12), 4236–4246. [PubMed: 23152977]

(14). Zhou H; Cheng C; Qin H; Ma L; He C; Nie S; Zhang X; Fu Q; Zhao C Self-Assembled 3d Biocompatible and Bioactive Layer at the Macro-Interface Via Graphene-Based Supermolecules. Polym. Chem 2014, 5 (11), 3563–3575.

(15). Li D; Müller MB; Gilje S; Kaner RB; Wallace GG Processable Aqueous Dispersions of Graphene Nanosheets. Nat. Nanotechnol 2008, 3 (2), 101–105. [PubMed: 18654470]

(16). Yang X; Wang Y; Huang X; Ma Y; Huang Y; Yang R; Duan H; Chen Y Multi-Functionalized Graphene Oxide Based Anticancer Drug-Carrier with Dual-Targeting Function and Ph-Sensitivity. J. Mater. Chem 2011, 21 (10), 3448–3454.

(17). Zhang W; Guo Z; Huang D; Liu Z; Guo X; Zhong H Synergistic Effect of Chemo-Photothermal Therapy Using Pegylated Graphene Oxide. Biomaterials 2011, 32 (33), 8555–8561. [PubMed: 21839507]

(18). Liu J; Fu S; Yuan B; Li Y; Deng Z Toward a Universal “Adhesive Nanosheet” for the Assembly of Multiple Nanoparticles Based on a Protein-Induced Reduction/Decoration of Graphene Oxide. J. Am. Chem. Soc 2010, 132 (21), 7279–7281. [PubMed: 20462190]

(19). Zhou X; Huang X; Qi X; Wu S; Xue C; Boey FY; Yan Q; Chen P; Zhang H In Situ Synthesis of Metal Nanoparticles on Single-Layer Graphene Oxide and Reduced Graphene Oxide Surfaces. J. Phys. Chem. C 2009, 113 (25), 10842–10846.

(20). Chen W; Yi P; Zhang Y; Zhang L; Deng Z; Zhang Z Composites of Aminodextran-Coated Fe3o4 Nanoparticles and Graphene Oxide for Cellular Magnetic Resonance Imaging. ACS Appl. Mater. Interfaces 2011, 3 (10), 4085–4091. [PubMed: 21882840]

(21). Yang K; Hu L; Ma X; Ye S; Cheng L; Shi X; Li C; Li Y; Liu Z Multimodal Imaging Guided Photothermal Therapy Using Functionalized Graphene Nanosheets Anchored with Magnetic Nanoparticles. Adv. Mater 2012, 24 (14), 1868–1872. [PubMed: 22378564]

(22). Ma X; Tao H; Yang K; Feng L; Cheng L; Shi X; Li Y; Guo L; Liu Z A Functionalized Graphene Oxide-Iron Oxide Nanocomposite for Magnetically Targeted Drug Delivery, Photo-thermal Therapy, and Magnetic Resonance Imaging. Nano Res. 2012, 5 (3), 199–212.

(23). Burke A; Ding XF; Singh R; Kraft RA; Levi-Polyachenko N; Rylander MN; Szot C; Buchanan C; Whitney J; Fisher J; Hatcher HC; D’Agostino R; Kock ND; Ajayan PM; Carroll DL; Akman S; Torti FM; Torti SV Long-Term Survival Following a Single Treatment of Kidney Tumors with Multiwalled Carbon Nanotubes and near-Infrared Radiation. Proc. Natl. Acad. Sci. U. S. A 2009, 106 (31), 12897–12902. [PubMed: 19620717]

(24). Gu Y; Chen WR; Xia M; Jeong SW; Liu H Effect of Photothermal Therapy on Breast Tumor Vascular Contents: Non-invasive Monitoring by near-Infrared Spectroscopy. Photochem. Photobiol 2005, 81 (4), 1002–1009. [PubMed: 15807632]

(25). Shah J; Park S; Aglyamov S; Larson T; Ma L; Sokolov K; Johnston K; Milner T; Emelianov SY Photoacoustic Imaging and Temperature Measurement for Photothermal Cancer Therapy. J. Biomed. Opt 2008, 13 (3), 034024. [PubMed: 18601569]

(26). Shah J; Aglyamov SR; Sokolov K; Milner TE; Emelianov SY Ultrasound Imaging to Monitor Photothermal Therapy–Feasibility Study. Opt. Express 2008, 16 (6), 3776–3785. [PubMed: 18542473]

(27). Stafford RJ; Shetty A; Elliott AM; Schwartz JA; Goodrich GP; Hazle JD Mr Temperature Imaging of Nanoshell Mediated Laser Ablation. Int. J. Hyperthermia 2011, 27 (8), 782–790. [PubMed: 22098362]

(28). Whitney JR; Rodgers A; Harvie E; Carswell WF; Torti S; Puretzky AA; Rouleau CM; Geohegan DB; Rylander CG; Rylander MN Spatial and Temporal Measurements of Temperature and Cell Viability in Response to Nanoparticle-Mediated Photo-thermal Therapy. Nanomedicine (London, U. K.) 2012, 7 (11), 1729–1742.

(29). Yoshikawa K; Nakata Y; Yamada K; Nakagawa M Early Pathological Changes in the Parkinsonian Brain Demonstrated by Diffusion Tensor Mri. J. Neurol., Neurosurg. Psychiatry 2004, 75 (3), 481–484. [PubMed: 14966170]

(30). Hamstra DA; Rehemtulla A; Ross BD Diffusion Magnetic Resonance Imaging: A Biomarker for Treatment Response in Oncology. J. Clin. Oncol 2007, 25 (26), 4104–4109. [PubMed: 17827460]

(31). Patterson DM; Padhani AR; Collins DJ Technology Insight: Water Diffusion Mri–a Potential New Biomarker of Response to Cancer Therapy. Nat. Clin. Pract. Oncol 2008, 5 (4), 220–233. [PubMed: 18301415]

(32). Norris DG; Niendorf T; Leibfritz D Healthy and Infarcted Brain Tissues Studied at Short Diffusion Times: The Origins of Apparent Restriction and the Reduction in Apparent Diffusion Coefficient. NMR Biomed. 1994, 7 (7), 304–310. [PubMed: 7718430]

(33). Szafer A; Zhong J; Gore JC Theoretical Model for Water Diffusion in Tissues. Magn. Reson. Med 1995, 33 (5), 697–712. [PubMed: 7596275]

(34). Le Bihan D; Turner R; Douek P; Patronas N Diffusion Mr Imaging: Clinical Applications. AJR, Am. J. Roentgenol 1992, 159 (3), 591–599. [PubMed: 1503032]

(35). Cheng HL; Haider MA; Dill-Macky MJ; Sweet JM; Trachtenberg J; Gertner MR Mri and Contrast-Enhanced Ultrasound Monitoring of Prostate Microwave Focal Thermal Therapy: An in Vivo Canine Study. J. Magn. Reson. Imaging 2008, 28 (1), 136–143. [PubMed: 18581405]

(36). Pilatou MC; Stewart EA; Maier SE; Fennessy FM; Hynynen K; Tempany CM; McDannold N Mri-Based Thermal Dosimetry and Diffusion-Weighted Imaging of Mri-Guided Focused Ultrasound Thermal Ablation of Uterine Fibroids. J. Magn. Reson. Imaging 2009, 29 (2), 404–411. [PubMed: 19161196]

(37). Yang K; Zhang SA; Zhang GX; Sun XM; Lee ST; Liu ZA Graphene in Mice: Ultrahigh in Vivo Tumor Uptake and Efficient Photothermal Therapy. Nano Lett. 2010, 10 (9), 3318–3323. [PubMed: 20684528]

(38). Liu XW; Tao HQ; Yang K; Zhang SA; Lee ST; Liu ZA Optimization of Surface Chemistry on Single-Walled Carbon Nanotubes for in Vivo Photothermal Ablation of Tumors. Biomaterials 2011, 32 (1), 144–151. [PubMed: 20888630]

(39). Chertok B; Moffat BA; David AE; Yu F; Bergemann C; Ross BD; Yang VC Iron Oxide Nanoparticles as a Drug Delivery Vehicle for Mri Monitored Magnetic Targeting of Brain Tumors. Biomaterials 2008, 29 (4), 487–496. [PubMed: 17964647]

(40). Eggener SE; Scardino PT; Carroll PR; Zelefsky MJ; Sartor O; Hricak H; Wheeler TM; Fine SW; Trachtenberg J; Rubin MA; Ohori M; Kuroiwa K; Rossignol M; Abenhaim L International Task Force on Prostate, C.; the Focal Lesion, P., Focal Therapy for Localized Prostate Cancer: A Critical Appraisal of Rationale and Modalities. J. Urol 2007, 178 (6), 2260–2267. [PubMed: 17936815]

(41). Cui Y; Zhang XP; Sun YS; Tang L; Shen L Apparent Diffusion Coefficient: Potential Imaging Biomarker for Prediction and Early Detection of Response to Chemotherapy in Hepatic Metastases. Radiology 2008, 248 (3), 894–900. [PubMed: 18710982]

(42). Liu Z; Robinson JT; Sun X; Dai H Pegylated Nanographene Oxide for Delivery of Water-Insoluble Cancer Drugs. J. Am. Chem. Soc 2008, 130 (33), 10876–10877. [PubMed: 18661992]

(43). Sun H; Cao L; Lu L Magnetite/Reduced Graphene Oxide Nanocomposites: One Step Solvothermal Synthesis and Use as a Novel platform for Removal of Dye Pollutants. Nano Res. 2011, 4 (6), 550–562.

(44). Maeda H The Enhanced Permeability and Retention (Epr) Effect in Tumor Vasculature: The Key Role of Tumor-Selective Macromolecular Drug Targeting. Adv. Enzyme Regul 2001, 41, 189–207. [PubMed: 11384745]

(45). Yang K; Feng LZ; Shi XZ; Liu Z Nano-Graphene in Biomedicine: Theranostic Applications. Chem. Soc. Rev 2013, 42 (2), 530–547. [PubMed: 23059655]

(46). Tong L; Zhao Y; Huff TB; Hansen MN; Wei A; Cheng JX Gold Nanorods Mediate Tumor Cell Death by Compromising Membrane Integrity. Adv. Mater 2007, 19, 3136–3141. [PubMed: 19020672]

(47). Chen CL; Kuo LR; Chang CL; Hwu YK; Huang CK; Lee SY; Chen K; Lin SJ; Huang JD; Chen YY In Situ Real-Time Investigation of Cancer Cell Photothermolysis Mediated by Excited Gold Nanorod Surface plasmons. Biomaterials 2010, 31 (14), 4104–4112. [PubMed: 20181393]

(48). Pattani VP; Shah J; Atalis A; Sharma A; Tunnell JW Role of Apoptosis and Necrosis in Cell Death Induced by Nanoparticle-Mediated Photothermal Therapy. J. Nanopart. Res 2015, 17 (1), 1–11.

(49). Monguzzi L; Ippolito D; Bernasconi DP; Trattenero C; Galimberti S; Sironi S Locally Advanced Rectal Cancer: Value of Adc Mapping in Prediction of Tumor Response to Radiochemotherapy. Eur. J. Radiol 2013, 82 (2), 234–240. [PubMed: 23122748]

(50). Melancon MP; Elliott A; Ji X; Shetty A; Yang Z; Tian M; Taylor B; Stafford RJ; Li C Theranostics with Multifunctional Magnetic Gold Nanoshells: Photothermal Therapy and T2* Magnetic Resonance Imaging. Invest. Radiol 2011, 46 (2), 132–140. [PubMed: 21150791]

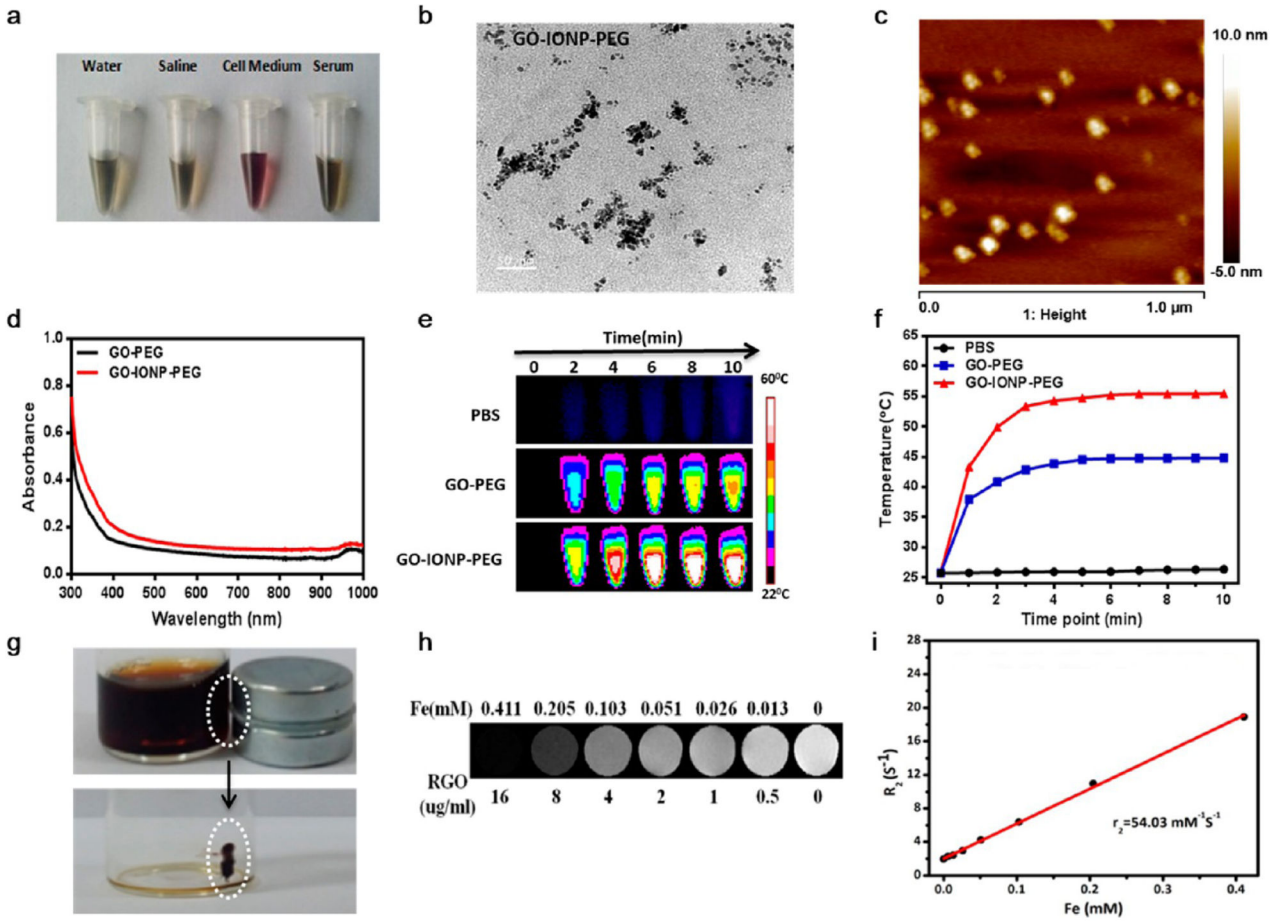

Figure 1.

Characterizations of GO-IONP-PEG. (a) Stability of GO-IONP-PEG in water, PBS, cell culture medium, and serum. (b) TEM image of GO-IONP-PEG. Scale bar: 50 nm. (c) AFM image of GO-IONP-PEG. Scale bar: 1 μm. (d) UV–vis–NIR absorbance spectra of GO-PEG and GO-IONP-PEG at the same GO concentration (10 μg/mL). (e) In vitro photothermal effect, evaluated with GO-IONP-PEG, GO-PEG, and PBS under 808 nm photoirradiation (0.5 W/cm^2 up to 10 min). GO-IONP-PEG and GO-PEG had the same GO concentration (30 μg/mL). (f) Temperature increase curves for GO-IONP-PEG, GO-PEG, and PBS, based on results from e. (g) Photographs showing the attraction of GO-IONP-PEG by a NdFeB magnet. Upper: before the magnet was applied. Under: after the magnetic separation. (h) T_2-weighted MR images of GO-IONP solutions with different iron concentrations. (i) On the basis of the results, a linear correlation between R_2 ($1/T_2$) and iron concentration was established to obtain r_2 (54.03 mM^{-1} s^{-1}).

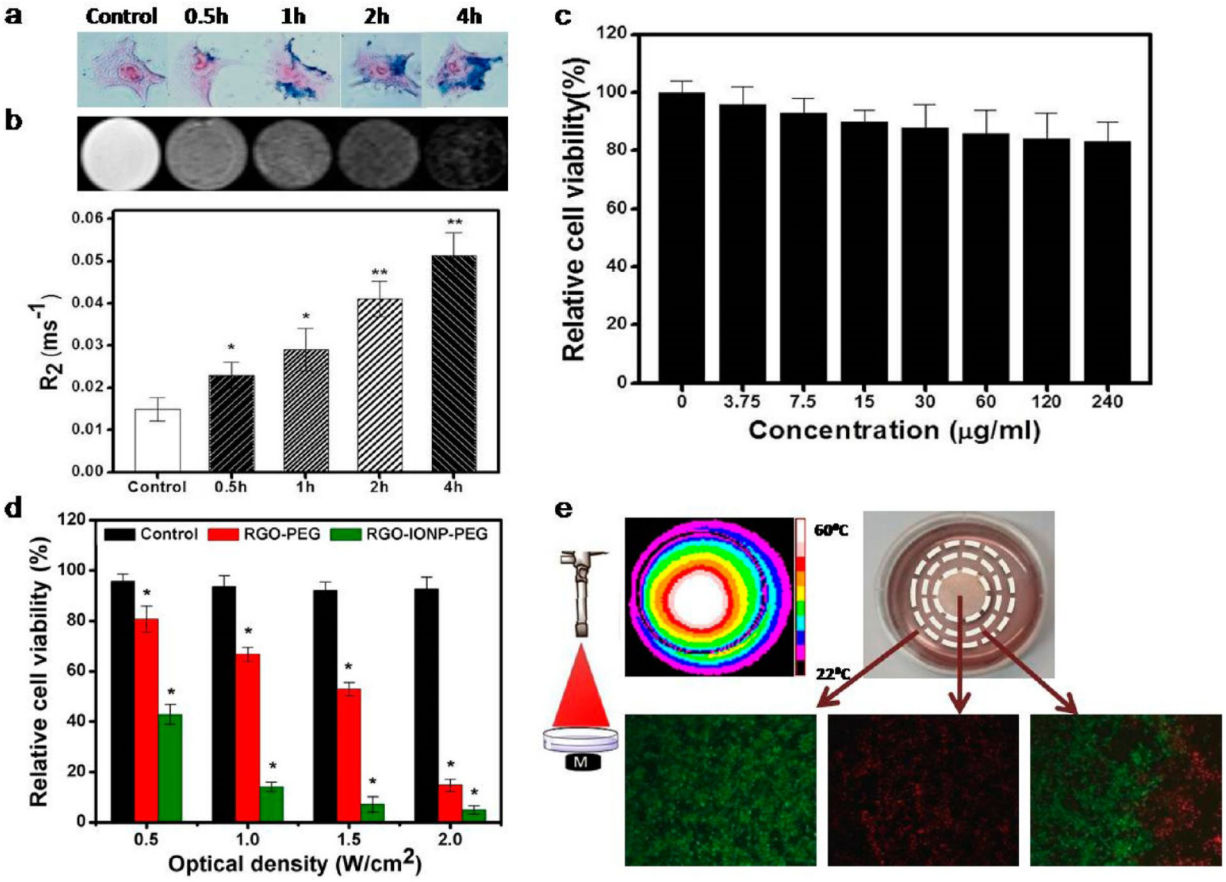

Figure 2.

Cell uptake and magnet-guided targeting. (a) Prussian blue staining. GO-IONP-PEG (100 μg/mL) was incubated with 4T1 cells for different times and the uptake was assessed by Prussian blue staining. (b) T_2-weighted images with agarose samples of cells from (a). Time dependent uptake led to increased R_2 values (*, $p < 0.05$; **, $p < 0.01$). (c) Cytotoxicity of GO-IONP-PEG, studied with 4T1 cells. The toxicity was assessed by standard MTT assay performed 24 h after the incubation. (d) PTT-induced cytotoxicity. 4T1 cells were incubated with GO-IONP-PEG (100 μg GO/mL), GO-PEG (100 μg GO/mL), or PBS for 12 h before irradiation by a 808 nm laser at different fluence rates (0.5 W/cm^2, 1.0 W/cm^2, 1.5 W/cm^2, 2.0 W/cm^2) for 10 min (*, $p < 0.05$). (e) Magnet-guided GO-IONP-PEG migration. A magnet was placed right under the center of a cell culture dish grown with 4T1 cells. After incubation with GO-IONP-PEG (100 μg/mL) for 4 h, an 808 nm laser was applied to cover the whole plate (1.0 W/cm^2 for 5 min). Temperature increase and cell death was observed in central, particle-rich zone but not in the peripheral region. Green, calcein AM (ex/em: 494/517 nm); red, PI (ex/em: 517/617 nm).

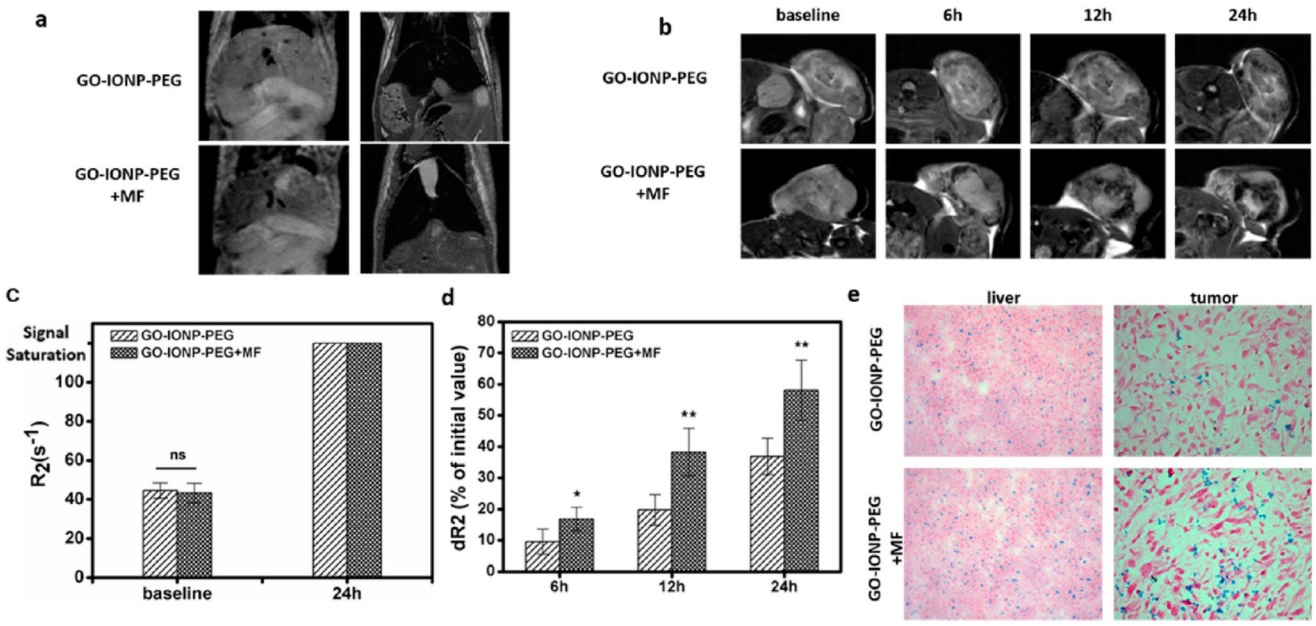

Figure 3.

In vivo MR imaging ($n = 5$). (a) T_2-weighted MR images of the mouse liver. The images were taken 24 h after intravenous injection of GO-IONP-PEG, with or without an external magnetic field (MF). (b) T_2-weighted MR images of tumors. Relative to the prescans, signal reduction was observed in tumors after GO-IONP-PEG injection, and the reduction level was gradually elevated. When there was a magnet attached to the tumor (bottom), the signal reduction was enhanced. (c) Quantitative analysis of R_2 in the liver before and 24 h after the particle injection, based on the imaging results from panel a. ns: no statistical difference. (d) Quantitative analysis of relative R_2 change (dR_2) at 6, 12, and 24 post injection, based on the imaging results from (b). Significant R_2 increase was observed when an external magnetic field was applied (*, $p < 0.05$; **, $p < 0.01$). (e) Prussian blue staining with liver and tumor samples. Although the liver uptake was comparable, using a magnet led to enhanced particle accumulation in the tumor.

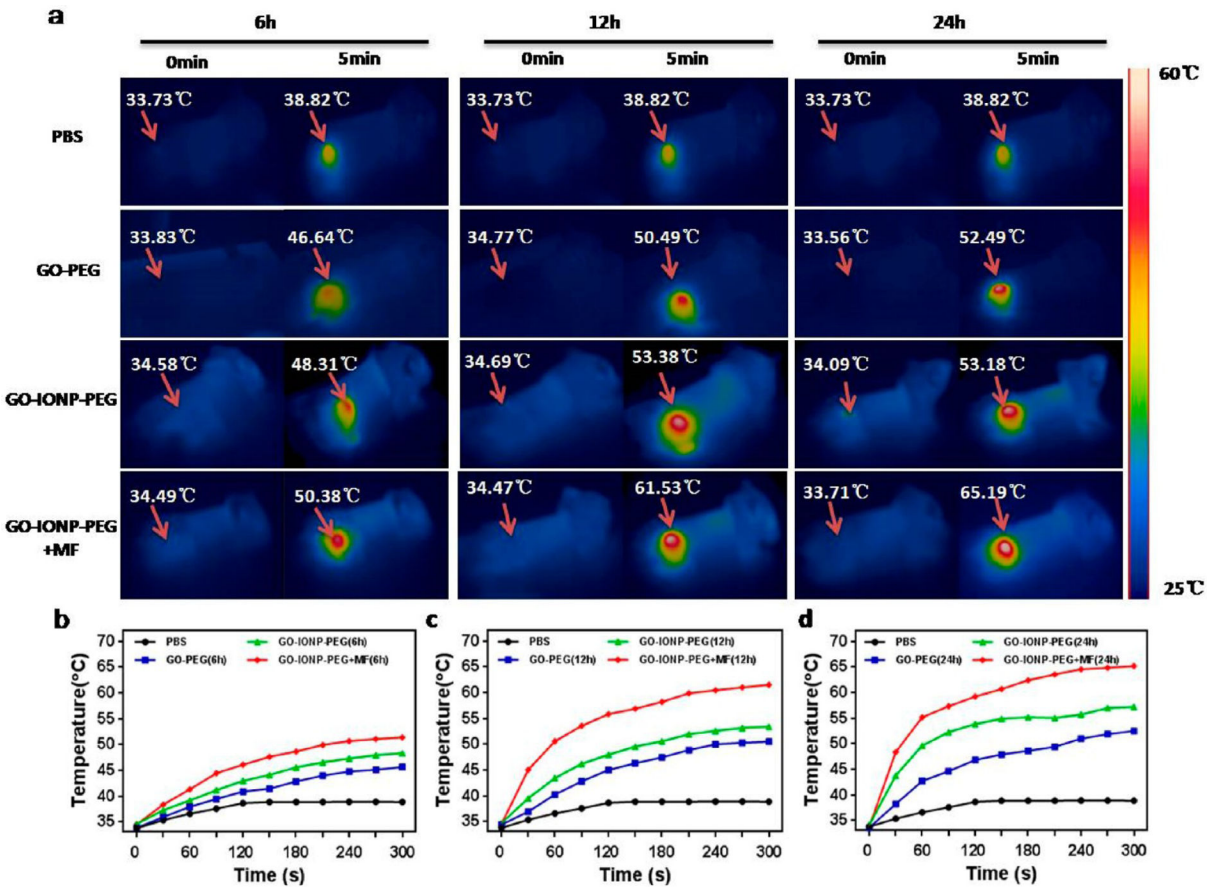

Figure 4.

In vivo photothermal effect. (a) Thermal images of 4T1 tumor-bearing mice treated with PBS, GO-PEG, GO-IONP-PEG, and GO-IONP-PEG+MF along with photoirradiation. An 808 nm laser (2 W/cm^2, 5 min) was applied at 6, 12, and 24 h postinjection in each group. (b–d) Temperature increase curves for the animals from panel a.

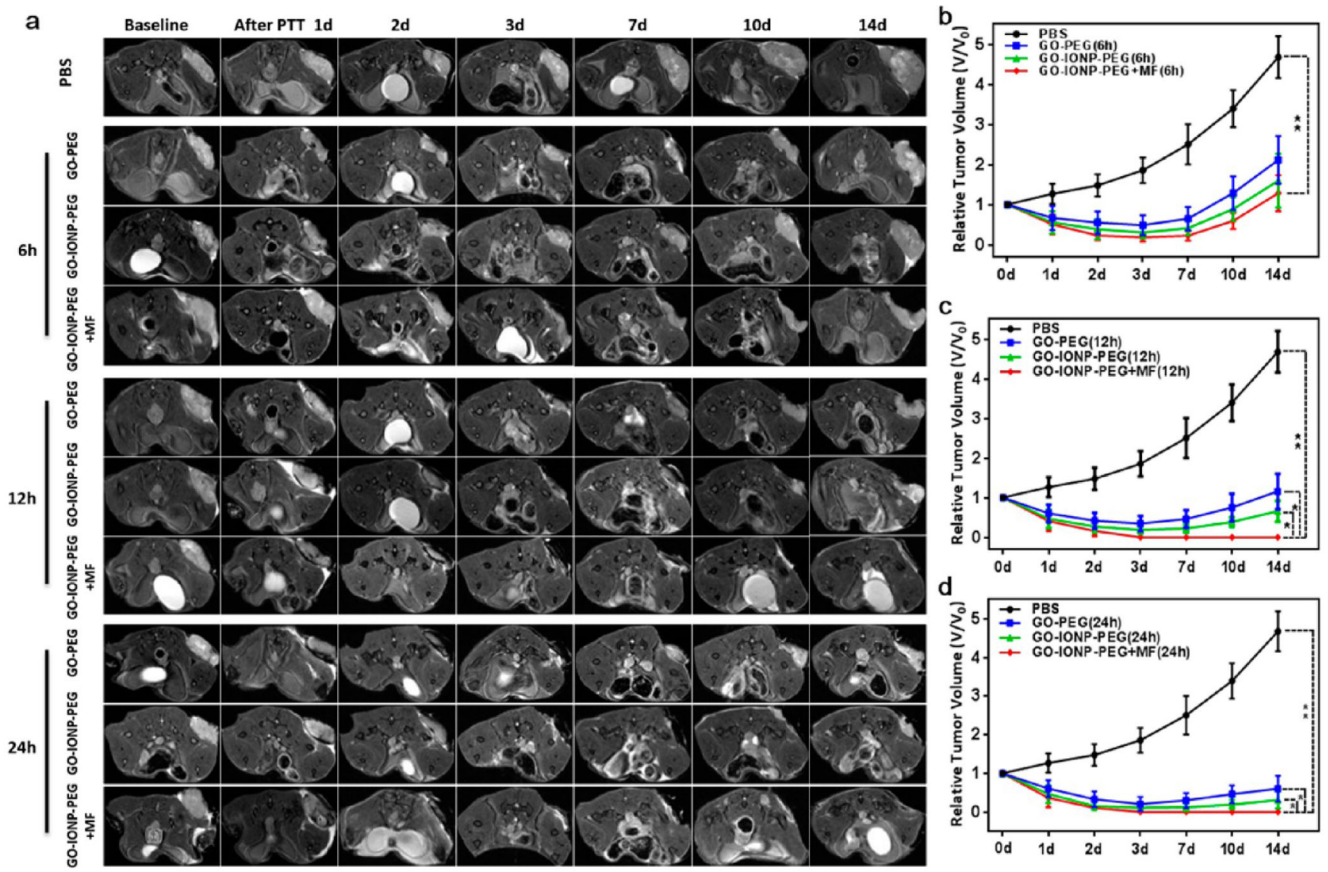

Figure 5.

T_2-weighted MRI to monitor tumor growth after PTT. (a) T_2-weighted MR images taken at different time points after PTT. (b–d) Tumor growth curves for different therapy groups (*, $p < 0.05$; **, $p < 0.01$).

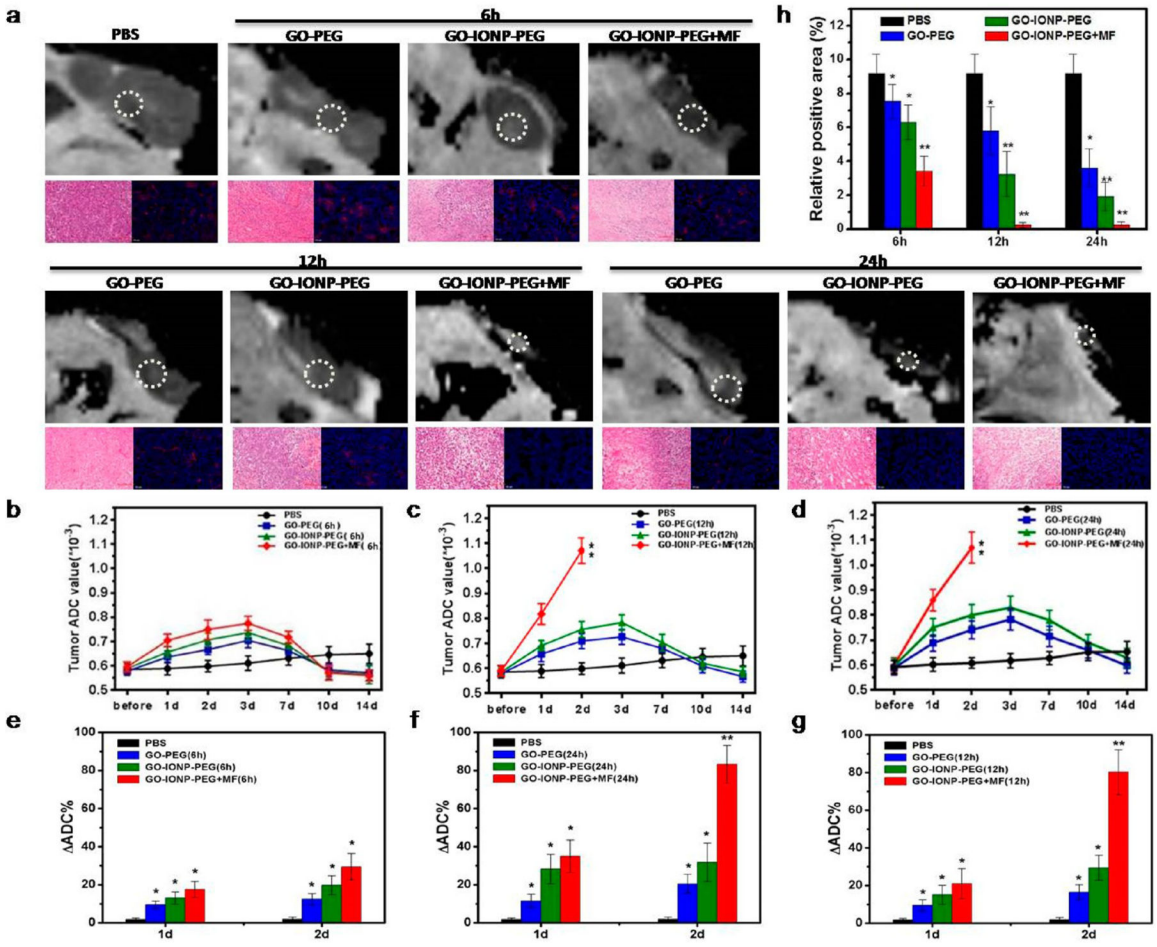

Figure 6.

DW-MRI to monitor therapy response. (a) DW-MR imaging as well as H&E and CD31 staining with tumors after PTT treatments. (b–d) Tumor ADC values, measured from DW-MRI results taken at different time points after PTT. Aside from the PBS groups, all of the animals showed increased tumor ADC values after PTT. The most dramatic increase was observed when GO-IONP-PEG was applied in conjugation with an external magnetic field and the tumors irradiated at either 12 or 24 h. (e–g) Relative ADC increase ΔADC%) on day 1 and day 2 after PTT. For the GO-IONP-PEG+MF (12 h) and GO-IONP-PEG+MF (24 h) groups, ΔADC% was found to be increased by over 80% on day 2. (h) Quantitative analysis of CD31-positive areas using ImageJ (*, $p < 0.05$; **, $p < 0.01$).

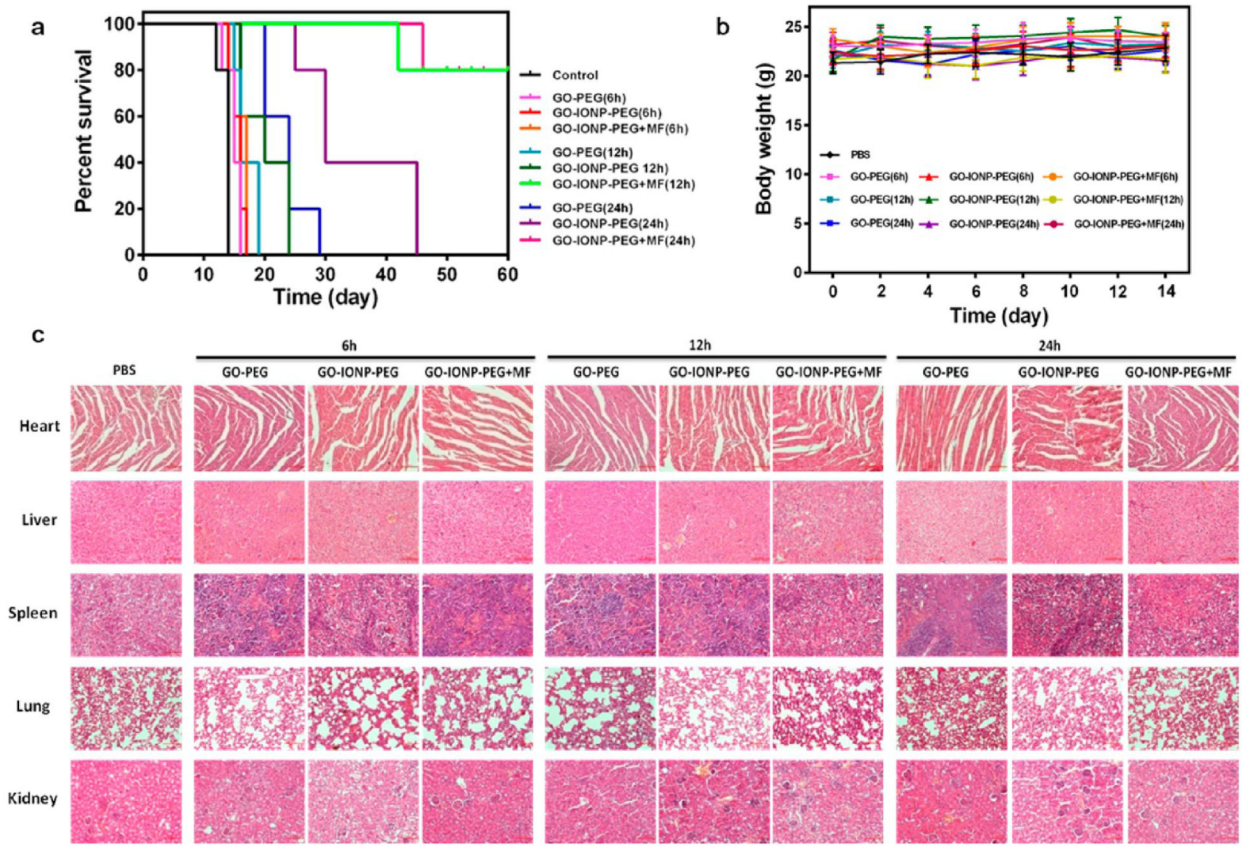

Figure 7.

Survival and histology results. (a) The survival curves of all the therapy groups. GO-IONP-PEG+MF (12 h) and GO-IONP-PEG+MF (24 h) groups showed the best survival rates, with 80% animals staying alive after 60 days. (b) Body weight curves. No significant weight loss was observed for all of the treatment groups. (c) H&E staining of major organs from all treatment groups. No detectable toxicity was observed in the heart, liver, spleen, lung, and kidneys.

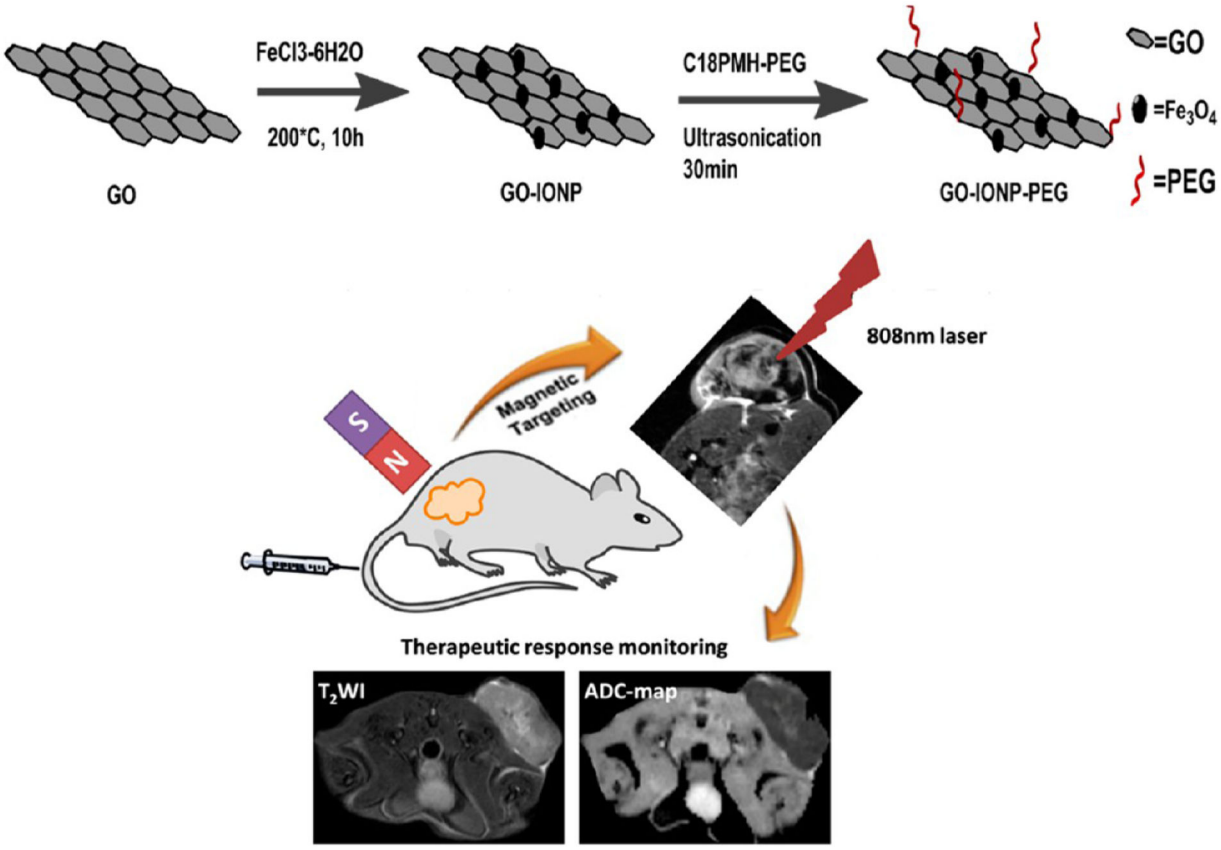

Scheme 1.

Schematic Illustration of the Experimental Design[a].

[a]GO-IONP-PEG was prepared by PEGylation of IONP-deposited GO nanosheets. GO-IONP-PEG was systematically administered into tumor bearing animals. The tumor targeting could be facilitated by an external magnetic field applied to the tumor area. Under photo-irradiation, the GO-IONP-PEG mediated PTT was inflicted on cancer cells. The therapy response was monitored by both T_2-weighted MRI and DW-MRI.